Simulation method of Wolter type I grazing incidence telescope imaging of an X-ray region

Peng Liu[1,2], Bo Chen[1], Ya-Chao Zhang[1,2], Ling-Ping He[1] and Xiao-Dong Wang[1]

[1] Changchun Institute of Optics, Fine Mechanics and Physics, Chinese Academy of Sciences, Jilin 130033, China; *liupengsbc@msn.cn*
[2] University of Chinese Academy of Sciences, Beijing 100049, China

Abstract This paper presents a method for simulating Wolter type I grazing incidence telescope imaging of an X-ray region. The imaging quality of a soft X-ray telescope is mainly affected by geometric aberrations, surface scatter and alignment errors. Using a Legendre-Fourier polynomial to fit the figure errors in the cylindrical coordinate system, the geometry of the mirror barrel with the figure errors can be modeled by the User Defined Object in ZEMAX. Based on the Harvey-Shack surface scatter theory, surface scatter is achieved by the Bidirectional Scatter Distribution Function (BSDF) scattering model. The alignment errors are calculated by a combination of experiment and simulation according to the shape of the spot resulting from the finite distance imaging experiment. By combining these factors that affect image quality, the telescope imaging of an infinity point is simulated by ZEMAX. According to the simulation results, the angular resolution of the telescope is calculated to be less than or equal to $1.86'$ at a wavelength of $1.33\,\mathrm{nm}$. The simulation method improves the ability of ZEMAX to simulate grazing incidence telescope imaging. This is of great significance for the research and manufacture of X-ray grazing incidence telescopes.

Key words: telescopes — scattering — methods: miscellaneous

1 INTRODUCTION

The Sun is the source of space weather. When a solar eruption occurs, a large amount of plasma, high-energy particles and radiation is hurled into space. Their interactions with the Earth's magnetosphere and ionosphere will disturb the Earth's space environment, potentially resulting in disastrous space weather. This has a serious impact on normal human activities (Li et al. 2005), such as the operation of satellites in orbit, astronaut spacewalk, GPS positioning, satellite communications, transmission networks, etc. A Wolter type I grazing incidence soft X-ray telescope (SXT) is one of the most important instruments for exploring the mechanisms of solar activities and forecasting space weather. It has been utilized to successfully perform solar observation tasks in several satellites, such as *Yohkoh* (Acton et al. 1991), *GOES-M* (Bornmann et al. 1996), *Hinode* (Suematsu et al. 2017), etc.

To ensure that the telescope can accurately locate and clearly observe the area of solar activity in orbit, it is necessary to characterize its resolution before launch. Resolution detection requires a uniform beam of parallel beams covering the entire telescope aperture. Parallel beams are generally obtained by imaging a point-like source at infinity using a collimator. However, the X-ray reflectance is extremely small in the case of normal incidence and it is not possible to generate a parallel beam by using a collimator. The ideal way to test an X-ray telescope is to create an artificial point-like X-ray star at infinite distance, which provides a wide collimated parallel X-ray beam. However, facilities producing collimated and uniform X-ray beams are very hard to build. The easiest way to meet these requirements is to put a point-like isotropic X-ray source as far as possible in front of the mirror system. An approximately parallel beam that fully covers the telescope aperture is generated by the X-ray source for resolution detection. The X-ray test facility at the Marshall Space Flight Center (West et al. 2011) implements this method, with a distance of $500\,\mathrm{m}$ between the X-ray source and telescopes. In addition, the X-ray test facility at the Institute of Space and Aeronautical Science in Japan (Kunieda et al. 1993; Shibata et al. 2001; Iizuka et al. 2018) uses a $30\,\mathrm{m}$ X-ray pencil beam with a width of $1\,\mathrm{mm}$ to fully scan the aperture of the telescope, and the resolution is obtained by

adding up all the scanning results. However, the first X-ray test facility is bulky and quite costly to build. Although the second test facility is relatively small in volume, the process of scanning the telescope aperture with a pencil beam is very time consuming.

To measure the resolution of the telescope more easily and at a lower cost, this paper proposes a method that does not require a giant test facility. The Wolter type I telescope imaging is simulated by ZEMAX. The operating waveband resolution of the telescope is obtained based on the results of experiment and simulation.

2 PRINCIPLE OF SIMULATION

The image quality of the Wolter type I telescope is degraded by a variety of factors, such as aperture diffraction, geometric aberrations, surface scatter, alignment errors and all other potential errors. The first four items are the main factors affecting image quality. Since the X-ray wavelength is very short, the effect of aperture diffraction on the X-ray telescope is almost negligible. So, we only consider the other three factors in the simulation process. The geometric aberration includes two parts: design residual and figure errors.

First, we need to model the mirror barrel of the grazing incidence telescope with figure errors. Because the obscuration ratio of a Wolter type I telescope is relatively large, relying on a Zernike polynomial to describe the figure errors is not suitable. The addition of figure errors is more difficult. In ZEMAX, an arbitrarily shaped object can be created by a User Defined Object. The User Defined Object is a compiled function (strictly speaking, a Windows dynamic-link library (DLL)) that can implement any surface shape, phase, transmission function or gradient index, and any combination of these that you wish, but the equation describing the shape of the object must be known. To solve this problem, the Legendre-Fourier (L-F) polynomial (Glenn 1984; Saha 1990) orthogonal in the cylindrical coordinate system is applied to describe the figure errors. The internal surface equation of the mirror barrel is given as

$$r(z, \theta) = \sqrt{2(z + z_0)/c - (1 + k)(z + z_0)^2} + h_{\text{error}}(z, \theta), \tag{1}$$

where z is the axial coordinate of the mirror barrel, r is the radial coordinate, θ is the azimuth angle, z_0 is the axial coordinate of the apex of the conic curve, c is the curvature of the vertex and k is the conic coefficient. $h_{\text{error}}(z, \theta)$ is a set of L-F polynomials used to describe the figure errors.

Its expression is as follows

$$h_{\text{error}}(z, \theta) = \sum_{n=0} \left\{ a_n P_n(Z) + \sum_{m=1} \left[b_{nm} P_n(Z) \cos(m\theta) \right. \right.$$
$$\left. \left. + c_{nm} P_n(Z) \sin(m\theta) \right] \right\}, \tag{2}$$

where $P_n(Z) = P_n(2(z - z_c)/L)$ is the nth Legendre polynomial, a_{n}, b_{nm} and c_{nm} are parameters of the L-F polynomial, L is the length of the axial direction of the mirror barrel, and z_c is the coordinate of the midpoint of the axial direction of the mirror barrel. Since the Legendre polynomial is orthogonal in the interval from -1 to $+1$, the axial coordinate z needs to be transformed to ensure the orthogonality of the polynomial. The figure errors of the mirror barrel are fitted using Equation (2). By inserting the fitting result into Equation (1), the equation of the mirror barrel with the figure errors can be obtained. The DLL file corresponding to the mirror barrel with the figure errors is obtained by compilation.

Second, a Bidirectional Scatter Distribution Function (BSDF) scattering model is established based on the Harvey-Shack surface scatter theory (Krywonos et al. 2011; Harvey 2015; Harvey & Pfisterer 2016) which employs the surface transfer function to characterize the scattering behavior of arbitrarily rough surfaces. The surface transfer function is calculated from the surface power spectral density (PSD) of the telescope. The Bidirectional Reflectance Distribution Function (BRDF) is obtained by the Fourier transform of the surface transfer function (Hamilton 2000). The BRDFs with different grazing incidence angles are then calculated and combined into a BSDF file (a file with the extension bsdf) which defines the scatter characteristics of the object surface. Using the BSDF file, the BSDF scattering model can be established on the surface of any object in non-sequence mode in ZEMAX.

Third, the alignment errors of the Wolter type I telescope optical system are limited to relative tilt, decenter and despace, as shown in Figure 1. The alignment errors are introduced to the optical system by changing the parameters of the secondary mirror in ZEMAX. For example, X Position and Y Position correspond to decenter, Z Position corresponds to despace, and Tilt about X and Tilt about Y correspond to tilt.

Finally, the telescope imaging is simulated in the ZEMAX non-sequence mode, and the resolution is calculated based on the simulation results. In non-sequential mode, the DLL files of the primary and secondary mirrors are loaded and the location parameters of the secondary mirror are set according to the alignment errors. We establish the BSDF scattering model and configure the reflectiv-
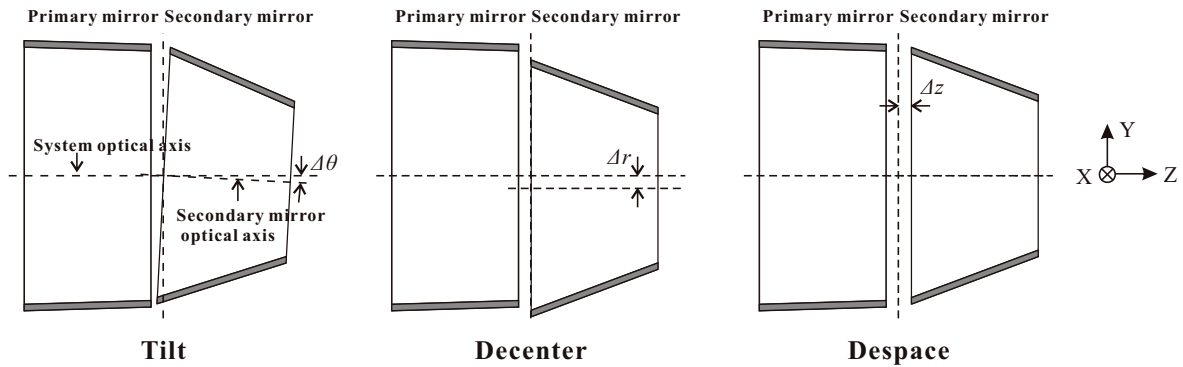
Fig. 1 Schematic diagram of alignment errors in the Wolter type I telescope optical system.
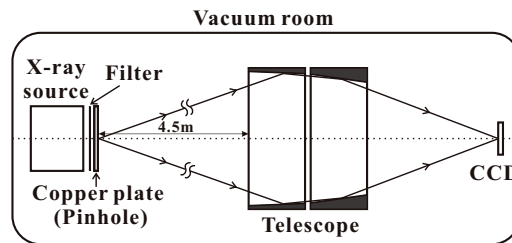

Fig. 2 Schematic of finite distance imaging experimental device.

Fig. 3 Image acquired by the finite distance imaging experiment at the X-ray band.

ity file in Object properties of the primary and secondary mirrors. In general, the reflectivity file needs to be calculated by ourselves based on the properties of the surface material of the mirror. After the source and detector are set, ray tracing can be performed. According to the tracing results, the operating waveband resolution of the telescope can be calculated.

3 CALCULATIONS OF THE ALIGNMENT ERRORS

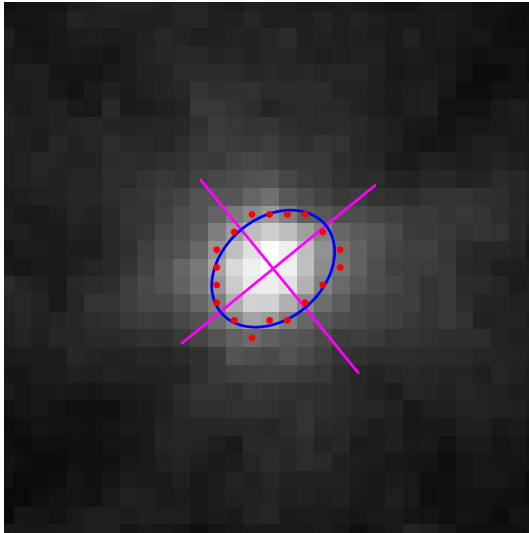### 3.1 Finite Distance Imaging Experiment

The real misalignment of the telescope is not available, but we can estimate it by indirect means. We performed a finite distance imaging experiment as illustrated in Figure 2. The alignment errors were calculated from the shape of the spot on the CCD. The main technical parameters of the Wolter type I telescope (Chen et al. 2004) used in the experiment are shown in Table 1.

The wavelength of the X-ray source is 1.33 nm. A copper plate with a small pinhole with a radius of 0.2 mm is fixed between the source and the telescope. Ideally, the pinhole is located on the optical axis of the telescope system. Under a visible light source, the experimental device was assembled so that the pinhole was located on the optical axis of the telescope. The deviation between the pinhole and the optical axis is less than 0.1 mm, which is very small compared with the distance of 4.5 m between the pinhole and the telescope. It has little effect on the imaging of the telescope, and the results compared with the ideal case are given later in the paper. The CCD was placed near the convergence of visible light and moved along the optical axis to find the minimum spot position. It is 765 mm from the joint of the telescope.

In a vacuum environment, X-rays passing through the pinhole were reflected by the telescope and finally fo-

Table 1 Technical Parameters of the Wolter Type I Telescope

Parameter Name	Numerical Value
Operating Waveband	0.6∼6.5 nm
Each Mirror Length	47.5 mm
Gap about Joint	5.0 mm
Radius at Joint	80 mm
Joint Focal Length	655 mm
Grazing Angle at Joint	1.74°
Vertex Radius (Paraboloid / Hyperboloid)	–2.43146 mm / –2.44047 mm
Conic Constant (Paraboloid / Hyperboloid)	–1.00 / –1.0074

Fig. 4 Edge distribution and fitting curve of the experimental spot at half height.

Table 2 Experimental Image Edge Fitting Results

Angle (°)	Major Axis Length (a) (pixel)	Minor Axis Length (b) (pixel)	a/b
39.25	7.80	5.77	1.35

Table 3 PV and RMS of the Residual Errors for Fitting Result of Grazing Incidence Telescope

	Primary Mirror	Secondary Mirror
PV (nm)	160.6	175.0
RMS (nm)	18.8	22.9

accurately measured. We utilized the Form Talysurf PGI 1000S and the NewView 6300 for surface measurement of the mirrors. Figure 5 plots the axial profile errors of the telescope with azimuth angles of 0° and 90° and the corresponding fitting curves. Figure 6 is the roundness of the section at the position of the primary and secondary mirror maximum diameters. It can be ascertained that the L-F polynomial not only fits well in the direction of the optical axis, but also fits well in the cross section of the vertical optical axis. The peak valley (PV) and root mean square (RMS) of the residual errors for the surface fitting result are listed in Table 3.

Figure 7 illustrates a surface PSD constructed from metrology data from the Wolter type I telescope mirror. Note that each metrology instrument is inherently band limited. Therefore, the surface PSD is pieced together from the results of measurements from separate metrology instruments. The equation of the PSD fitting curve and the value of the fitting parameter are expressed in Figure 7.

Based on the measured surface quality data of the mirrors, the DLL files of the primary and secondary mirrors with the figure errors and the BSDF scattering file were obtained by calculation and compilation.

3.3 Comparison between Simulation and Experiment

We first used ZEMAX to simulate the finite distance imaging of the telescope, and obtain an image that only considers the figure errors and an image that takes into account the figure errors and surface scatter. As with the processing of the experimental image, the edge of the light intensity at
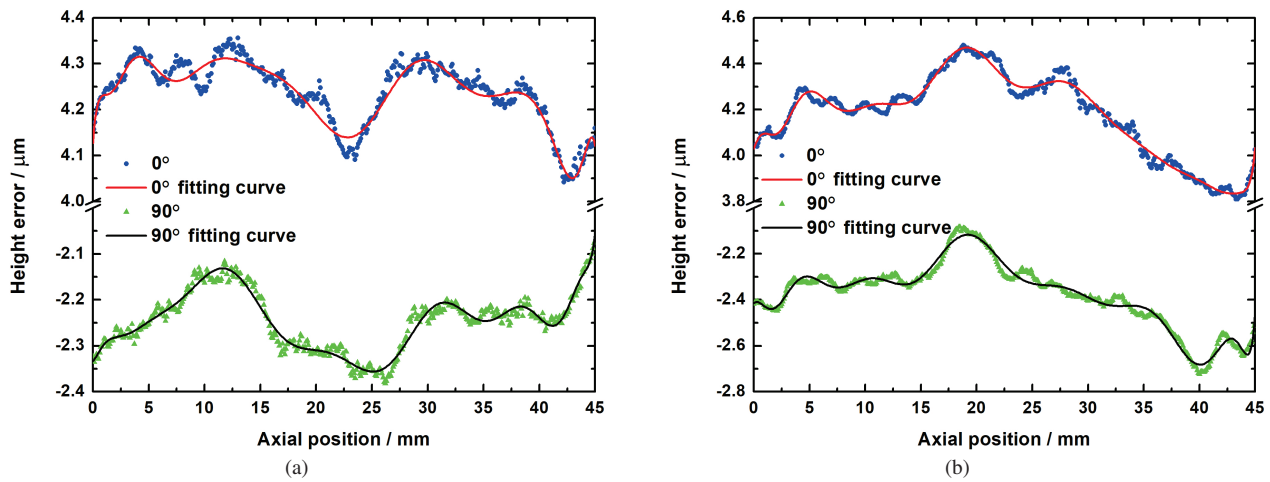
cused on an X-ray detector. Figure 3 displays a part of the image acquired by the detector with an imaging area of 151×151 pixels. The pixel size of the X-ray detector is 13.5×13.5 μm.

The scattering effect on the detector far away from the image point can be ignored, and its average intensity value is approximated as the intensity of the background noise. The light intensity of the image was normalized after the background noise was removed from the image. Edge detection was performed on the area of the image with a value greater than or equal to 0.5 using the Sobel operator. The red dots in Figure 4 are the edge pixel and the edge distribution is approximately elliptical. We applied the least squares method to fit the edge points to obtain the major axis, the minor axis and the angle between the minor axis and the vertical direction (Table 2). In Figure 4, the blue ellipse is the fitting curve and the crosshairs represent the direction of the major and minor axes.

3.2 Simulation Preparation

To exactly simulate the Wolter type I telescope imaging, the optical surface quality of the telescope mirror must be

Fig. 5 Axial profile errors of azimuth angle of 0 and 90 degrees for primary and secondary mirrors of grazing incidence telescope: (a) Primary mirror. (b) Secondary mirror.
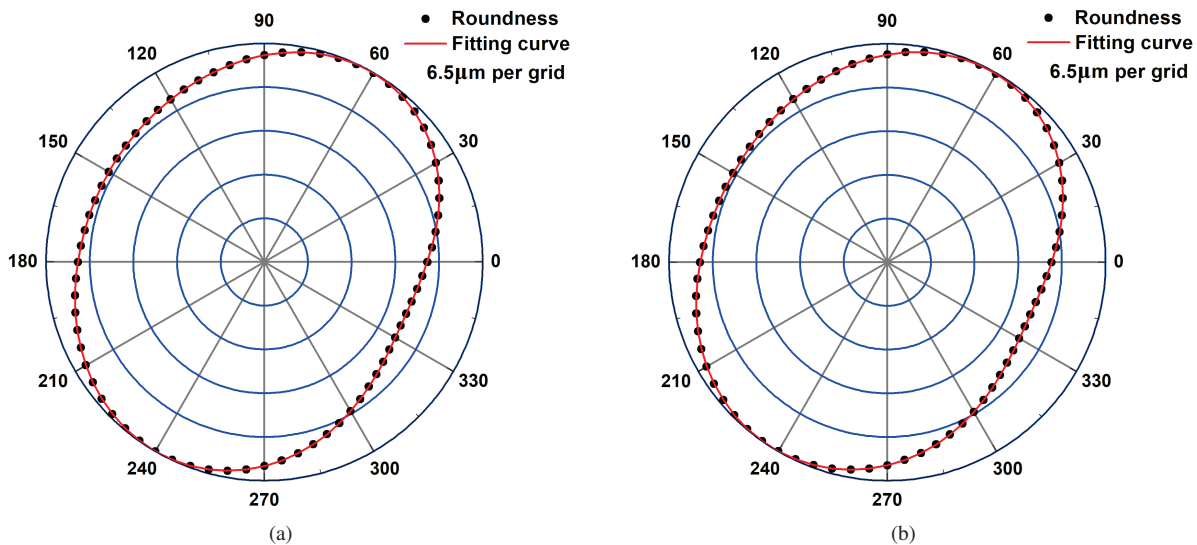

Fig. 6 Roundness of primary and secondary mirrors in grazing incidence telescope: (a) Primary mirror. (b) Secondary mirror.

Table 4 Fitting Results of Finite Distance Imaging under Different Conditions

	Angle (°)	Major Axis (a) (pixel)	Minor Axis (b) (pixel)	a/b
Figure Errors	35.54	5.47	4.59	1.19
Figure Errors + Scatter	40.55	6.14	6.04	1.02
Figure Errors + Scatter + despace (0.01 mm)	40.10	6.31	6.08	1.04
Figure Errors + Scatter + pinhole off-axis (0.1 mm)	40.27	6.33	6.10	1.04

half height was extracted and fitted. The results are exhibited in Figure 8 and Table 4. It is apparent from the results that the shape of the spot that considers the scattering effect is more rounded. The reason for this phenomenon is that the scattering effect dominates figure errors for the experi-

mental telescope. Therefore, we judged that the alignment errors are the cause of the experimental spot being oval.

The primary and secondary mirrors are processed on a Zerodur cylinder, and the axial machining error (despace) is no more than 0.01 mm. It can be seen from the results in
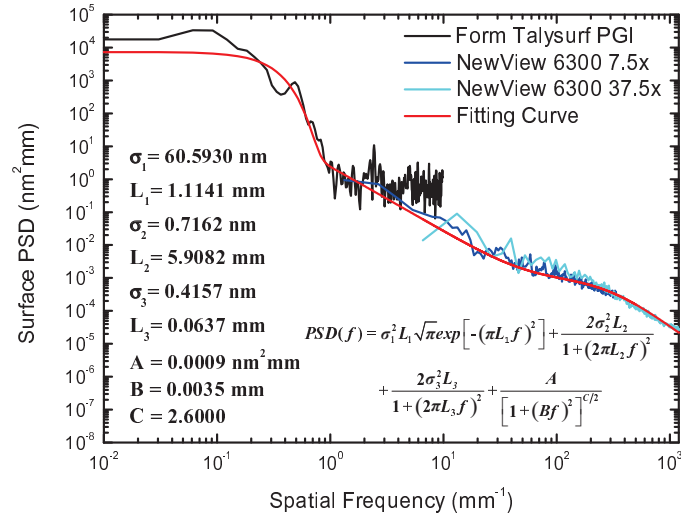
Fig. 7 Composite surface PSD function determined from two different metrology instruments.

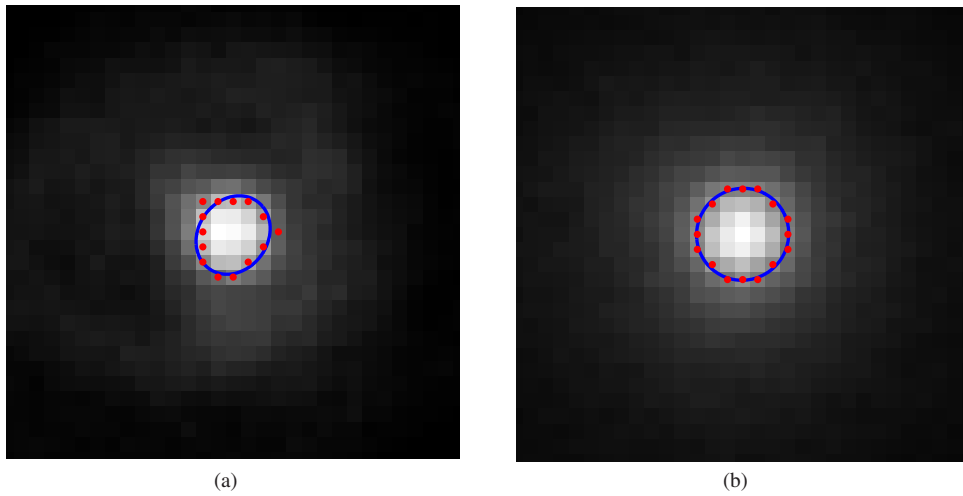(a)   (b)

Fig. 8 Simulation results of finite distance imaging under different conditions: (a) Only considering the figure errors. (b) Considering the figure errors and surface scatter.
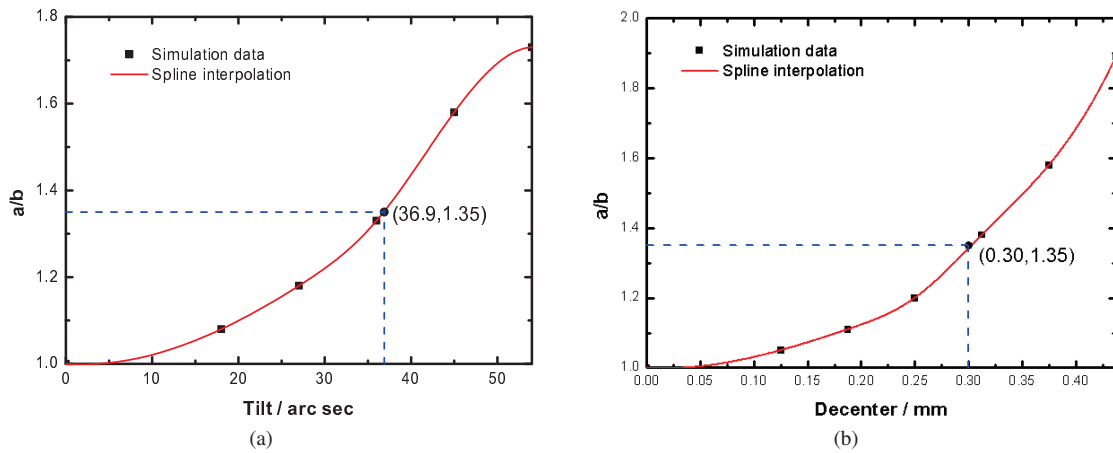

(a)   (b)

Fig. 9 The curve of a/b as a function of tilt or decenter: (a) a/b as a function of tilt. (b) a/b as a function of decenter.

Table 5 Spot Size Changes with Tilt

Tilt (″)	18	27	36	45	54
Major Axis Length (a) (pixel)	6.30	6.72	7.21	8.08	9.14
Minor Axis Length (b) (pixel)	5.83	5.69	5.41	5.10	5.27
a/b	1.08	1.18	1.33	1.58	1.73

Table 6 Spot Size Changes with Decenter

Decenter (mm)	0.125	0.1875	0.25	0.3125	0.375	0.4375
Major Axis Length (a) (pixel)	6.24	6.27	6.50	7.35	7.59	8.74
Minor Axis Length (b) (pixel)	5.93	5.64	5.42	5.33	4.80	4.62
a/b	1.05	1.11	1.20	1.38	1.58	1.89

Table 7 Comparison of Experimental and Simulation Results (relative errors in parentheses)

Tilt	Decenter	TD Angle	Major Axis Length (a) (pixel)	Minor Axis Length (b) (pixel)	a/b
Experiment			7.80	5.77	1.35
36.9″	0.00 mm		7.53 (3.46%)	5.45 (5.55%)	1.38 (2.22%)
0.0″	0.30 mm		7.16 (8.21%)	5.37 (6.93%)	1.33 (1.48%)
11.9″	0.20 mm	0°	6.91 (11.41%)	5.27 (8.67%)	1.31 (2.96%)
18.0″	0.15 mm	0°	7.07 (9.36%)	5.20 (9.88%)	1.36 (0.74%)
28.8″	0.10 mm	0°	7.98 (2.31%)	5.81 (0.69%)	1.37 (1.48%)
25.9″	0.21 mm	90°	7.57 (2.95%)	5.64 (2.25%)	1.34 (0.74%)
36.9″	0.30 mm	120°	7.18 (7.95%)	5.53 (4.16%)	1.30 (3.70%)
73.8″	0.30 mm	180°	7.49 (3.97%)	5.57 (3.47%)	1.34 (0.74%)
36.9″	0.48 mm	180°	6.81 (12.69%)	4.94 (14.38%)	1.38 (2.22%)

Table 4 that the effect of despace on the shape of the spot is small. The value of the major axis variation is the most, but the relative error is less than 2.8%. The simulation results of the pinhole, which is off-axis by 0.1 mm, indicate that the spot shape change is also small and the maximum relative error is less than 3.1%. Therefore, both of these errors are negligible.

We know that the angle between the minor axis of the experimental spot and the vertical direction is $39.25°$, and the distribution of light intensity in Figure 4 has a tendency to shift to the lower right. Studying the effects of decenter and tilt on the spot independently, we moved the secondary mirror along the minor axis of the experimental spot or tilted the secondary mirror in the plane determined by the z axis and the minor axis. Each time, we entered a different value in ZEMAX for ray tracing. Finally, we obtained the data that demonstrate the shape of the spot varies with tilt or decenter (Tables 5 and 6).

In Figure 9, the curve of a/b as a function of tilt (or decenter) is plotted and the data points are fitted using spline interpolation. According to the fitting result, when the a/b is equal to 1.35, the tilt angle is $36.9''$ and the decenter amount is 0.30 mm. It can be inferred from Table 5 and Table 6 that tilt and decenter have the same effect on the influence of a/b, for example, the a/b value with a tilt error of $27''$ is largely equal to the a/b value with a decenter error of 0.25 mm. As shown in Figure 9, the a/b value increases monotonically with the tilt or decenter. Regarding the influence of the a/b value, each tilt error corresponds to

a decenter error. The angle between tilt and decenter (TD Angle) is specified as the angle between the decenter error vector corresponding to the tilt error and the decenter error vector. We simulated several cases where tilt and decenter coexist, and the results are displayed in Table 7 (the relative errors are in parentheses).

4 RESOLUTION CALCULATION

In ZEMAX, the source was changed to a parallel light source, and then the secondary mirror was tilted or decentered according to the value calculated in the previous section. The image obtained by ray tracing was the light intensity distribution of the telescope point spread function (PSF). The encircled energy of the system is calculated from the PSF, and the results of the half power radius (HPR) are listed in Table 8. It can be seen from the table that the HPRs with different alignment errors are basically the same and their maximum value is $55.89''$. The angular resolution is twice the HPR value, so the operating waveband resolution of the telescope is less than or equal to $1.86'$.

5 CONCLUSIONS

To obtain the angular resolution of the Wolter I telescope for an X-ray region, we used ZEMAX to simulate the telescope imaging of the infinity point and obtain the PSF. According to the PSF, the operating waveband resolution of the telescope was calculated. Geometric aberrations,

Table 8 HPR of the Infinity Distance Imaging with Different Alignment Errors

Tilt	Decenter	TD Angle	HPR
36.9″	0.00 mm		51.08″
0.0″	0.30 mm		55.89″
11.9″	0.20 mm	0°	53.37″
18.0″	0.15 mm	0°	52.40″
28.8″	0.10 mm	0°	54.51″
25.9″	0.21 mm	90°	53.02″
36.9″	0.30 mm	120°	53.35″
73.8″	0.30 mm	180°	47.28″
36.9″	0.48 mm	180°	49.09″

surface scatter and alignment errors were considered in the simulation program. The modeling of the mirror barrel with the figure errors was realized by the L-F polynomial. By analyzing the finite distance imaging simulation results, the data on the spot shape as a function of the alignment errors were obtained. The alignment errors were estimated from the shape of the spot of the finite distance imaging experiment of the telescope. The alignment error was input into the simulation program, and the HPR of the telescope infinity imaging is calculated to be less than $55.89''$ at a wavelength of 1.33 nm. Finally, the operating waveband resolution of the telescope is less than or equal to $1.86'$. The proposed simulation method provides a method for evaluating the imaging quality of X-ray grazing incidence telescopes. This is of great significance for the research and manufacture of grazing incidence telescopes.

References

Acton, L., Bruner, M., Lemen, J., et al., 1991, Solar Physics, 136, 37

Bornmann, P. L., Speich, D., Hirman, J., et al. 1996, in Society of Photo-Optical Instrumentation Engineers (SPIE) Conference Series, 2812, GOES-8 and Beyond, ed. E. R. Washwell, 309

Bo, C., Chen, S.-Y., & Gong, Y. 2004, Optical Technique, 30, 242

Glenn, P. 1984, Optical Engineering, 23, 384

Hamilton, A. J. S. 2000, MNRAS, 312, 257

Harvey, J. E. 2015, Appl. Opt., 54, 2224

Harvey, J. E., & Pfisterer, R. N. 2016, in Proc. SPIE, 9961, Reflection, Scattering and Diffraction from Surfaces V, 996103

Iizuka, R., Hayashi, T., Maeda, Y., et al. 2018, Journal of Astronomical Telescopes, Instruments and Systems, 4, 011213

Krywonos, A., Harvey, J. E., & Choi, N. 2011, Journal of the Optical Society of America A, 28, 1121

Kunieda, H., Tsusaka, Y., Suzuki, H., et al. 1993, Japanese Journal of Applied Physics, 32, 4805

Li, B.-Q., Zhu, G.-W., Wang, S.-J., et al. 2005, Chinese J. Geophys. (in Chinese), 48, 235

Saha, T. T. 1990, Optical Engineering, 29, 1296

Shibata, R., Ishida, M., Kunieda, H., et al. 2001, Appl. Opt., 40, 3762

Suematsu, Y., Ichimoto, K., Katsukawa, Y., Tsuneta, S., & Shimizu, T. 2017, in Proc. SPIE, 10566, 105662Z

West, E., Pavelitz, S., Kobayashi, K., et al. 2011, in Proc. SPIE, 8147, 81471A